



**HAL**  
open science

# Overlapping two standing-waves in a microcavity for a multi-atom photon interface

Sebastien Garcia, Francesco Ferri, Jakob Reichel, Romain Long

► **To cite this version:**

Sebastien Garcia, Francesco Ferri, Jakob Reichel, Romain Long. Overlapping two standing-waves in a microcavity for a multi-atom photon interface. *Optics Express*, 2020, 28 (10), pp.15515. 10.1364/OE.392207 . hal-02850863

**HAL Id: hal-02850863**

**<https://hal.sorbonne-universite.fr/hal-02850863>**

Submitted on 7 Jun 2020

**HAL** is a multi-disciplinary open access archive for the deposit and dissemination of scientific research documents, whether they are published or not. The documents may come from teaching and research institutions in France or abroad, or from public or private research centers.

L'archive ouverte pluridisciplinaire **HAL**, est destinée au dépôt et à la diffusion de documents scientifiques de niveau recherche, publiés ou non, émanant des établissements d'enseignement et de recherche français ou étrangers, des laboratoires publics ou privés.

# Overlapping two standing-waves in a microcavity for a multi-atom photon interface

SÉBASTIEN GARCIA,<sup>1,2,†</sup> FRANCESCO FERRI,<sup>1,3</sup> JAKOB REICHEL,<sup>1</sup>  
AND ROMAIN LONG<sup>1,\*</sup>

<sup>1</sup> *Laboratoire Kastler Brossel, ENS-Université PSL, CNRS, Sorbonne Université, Collège de France, 24 rue Lhomond, 75005 Paris, France*

<sup>2</sup> *Present address: Young Physics team's, Institute of Physics, Collège de France, 11 place Marcelin Berthelot, 75005 Paris, France*

<sup>3</sup> *Present address: Institute for Quantum Electronics, ETH Zürich, 8093 Zürich, Switzerland*

<sup>†</sup>*sebastien.garcia@college-de-france.fr, \*long@lkb.ens.fr*

**Abstract:** We develop a light-matter interface enabling strong and uniform coupling between a chain of cold atoms and photons of an optical cavity. This interface is a fiber Fabry-Perot cavity, doubly resonant for both the wavelength of the atomic transition and for a geometrically commensurate red-detuned intracavity trapping lattice. Fulfilling the condition of a strong and uniform atom-photon coupling requires optimization of the spatial overlap between the two standing waves in the cavity. In a strong-coupling cavity, where the mode waists and Rayleigh range are small, we derive the expression of the optimal trapping wavelength taking into account the Gouy phase. The main parameter controlling the overlap of the standing waves is the relative phase shift at the reflection on the cavity mirrors between the two wavelengths, for which we derive the optimal value. We have built a microcavity optimized according to these results, employing custom-made mirrors with engineered reflection phase for both wavelengths. We present a method to measure with high precision the relative phase shift at reflection, which allows us to determine the spatial overlap of the two modes in this cavity.

© 2020 Optical Society of America under the terms of the [OSA Open Access Publishing Agreement](#)

## 1. Introduction

The development of light-matter interfaces has played a key role in the progress achieved in laser physics, nonlinear optics and quantum optics. In recent years, the emergence of quantum technologies underlines the need of developing new interfaces for applications ranging from quantum communication to quantum metrology. In Cavity Quantum Electrodynamics (CQED) [1], the light-matter coupling is enhanced by placing emitters inside a cavity. One prominent milestone in this field has been the achievement of the strong coupling regime between a single emitter and a cavity mode [2–8].

Focusing on atomic systems, single atoms strongly coupled to a cavity are envisioned as the elementary nodes of future quantum networks [9, 10]. The interaction between a cold atomic ensemble and a cavity mode in the weak coupling regime at the single atom level has led to the generation of multiparticle entangled states useful for metrology [11–13]. Light matter interfaces have also been pushed to explore the regime where each atom of an atomic ensemble is strongly coupled to the cavity mode. This allows to engineer a strong controllable effective coupling between the atoms mediated by the cavity field, enabling the generation of specific multiparticle entangled states [14, 15] and the simulation of many-body models [16–19].

For experiments with many atoms, the question arises on how to implement a strong and yet uniform coupling between the cavity mode and each atom of the atomic ensemble, which requires that all the atoms interact with the same maximal value of the cavity field. To implement this condition, one approach is to minimize the size of the atomic sample by using Bose-Einstein Condensates (BEC) and loading the BEC inside a single antinode of the cavity mode [20, 21].

This method is very effective for generating collective interaction but it is not compatible with single particle detection and control, which has emerged as a powerful tool in the fields of trapped ions [22], Rydberg atoms [23] and ultracold atoms in optical lattices [24]. In the context of CQED, single atom addressability has only been realized in systems with two atoms [15, 25].

In order to combine single particle resolution and a strong uniform coupling of each atom with the cavity mode resonant with the atomic transition, we use the spatial periodicity of the standing waves of linear Fabry-Perot cavity modes. By precisely positioning single atoms at different antinodes of the cavity mode, we can obtain a one-dimensional array of single atoms with maximal uniform coupling and single particle control. To get a stable overlap between the atoms and the cavity mode at the wavelength  $\lambda_1$  of the atomic transition, we aim to produce such a chain of atoms by optically trapping the atoms at the antinodes of a second red-detuned cavity mode at a commensurate wavelength  $\lambda_2 \simeq 2\lambda_1$ , as presented in Fig. 1. Such a configuration has been used previously to couple atomic ensemble to a macroscopic cavity in the weak coupling regime [19, 26–29].

In this article, we show that extending this scheme to atomic ensembles where each atom is strongly coupled to the cavity field necessitates a careful maximization of the spatial overlap between the two standing-waves of the doubly-resonant cavity. We demonstrate how to optimize this overlap, we present experimental methods to measure it and we apply them to our doubly-resonant cavity. The overlap is especially critical for CQED experiments in the strong coupling regime, as they usually require cavities with high finesse and small mode volume, which leads to the natural choice of microcavities such as fiber Fabry-Perot cavities [30]. For such short cavities, the Rayleigh range is usually small and so the Gouy phase shift plays a major role. In addition, the atomic ensemble spreads over a large fraction of the cavity length (on the order of the Rayleigh length), which imposes special constraints for the optimization. A similar problematic arises in frequency doubling by using a doubly-resonant cavity, where a good spatial overlap is also required between the fundamental mode and the second harmonic one [31–34]. But, microcavities are usually not used in this context, which relaxes the need for an advanced optimization of the overlap.

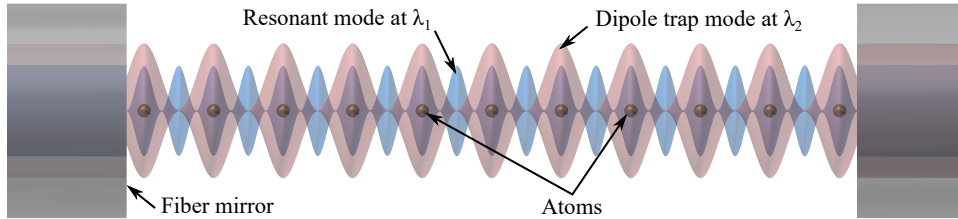


Fig. 1. Schematic view of our multi-atom photon interface in a fiber Fabry-Perot cavity (not to scale). The photonic mode (blue) of the quantum interface has a wavelength  $\lambda_1$  close to the atomic resonance. A second auxiliary cavity mode (red) with wavelength  $\lambda_2 \simeq 2\lambda_1$ , red-detuned from atomic resonance, creates an array of microtraps that overlap with each second maximum of the field at  $\lambda_1$ . This optimizes the coupling between the atomic array and the cavity photons at  $\lambda_1$ .

In section 2, we analyze theoretically the parameters that affect the overlap and we derive conditions to optimize it. In particular, we show in the following that the naive condition  $\lambda_2 = 2\lambda_1$  needs corrections due the geometric Gouy phase shift which leads to a non-trivial optimal wavelength for the trapping light. Given this condition, we demonstrate that the maximal overlap is obtained for an optimal relative phase shift between the two wavelengths at the reflection on the cavity mirrors. We illustrate the effect of this optimization by plotting the characteristic overlap phase and the strength of the coupling between a single atom and a photon for all trapping

positions along the cavity axis. In Sec. 3, we discuss the implementation of the optimal relative phase on reflection for our dielectric mirror coatings. Then, we report on experimental techniques which we developed to measure this relative phase. First in Sec. 4, we observe directly the overlap via the perturbation of the two modes at  $\lambda_1$  and  $\lambda_2$  with a nanoscopic probe and we deduce a coarse value of the relative phase. Second, in Sec. 5, we present a measurement that allows us to determine the relative phase with high precision, by measuring the double resonance condition as a function of the cavity length.

## 2. Doubly-resonant cavities with maximal spatial overlap of the standing waves

In this first part, we analyze and optimize the parameters that determine the spatial overlap of the modes in order to maximize it. We consider a linear Fabry-Perot resonator whose geometrical length is given by  $L$ , formed by two identical spherical concave mirrors, i.e. with identical radius of curvature  $R$  and identical coating. This configuration places the waist of the cavity modes at the center of the resonator and thus maximizes here the coupling to emitters. The following analysis can be extended to the case of asymmetric cavities where the two mirrors have different radii of curvature.

### 2.1. Optimal wavelength

In the simple case of plane waves, the maximal spatial overlap between the standing waves at  $\lambda_1$  and  $\lambda_2$  is simply obtained by the condition  $\lambda_2 = 2\lambda_1$ . For Gaussian cavity modes, we only consider in the following the fundamental transverse Gaussian mode  $\text{TEM}_{00}$ , so transverse coordinates are not involved. However, the Gouy phase shift has to be taken into account, which is the additional phase shift accumulated by a Gaussian beam when passing through its waist compared to an ideal plane wave. As a consequence, the effective wavelength of the Gaussian beam around the focus can be significantly different from  $c/\nu$ , where  $\nu$  is the laser frequency and  $c$  the speed of light. In order to obtain a maximal spatial overlap between the two wavelengths  $\lambda_1$  and  $\lambda_2 \approx 2\lambda_1$ , this local variation of the periodicity has to be taken into account to determine the optimal wavelength. By defining  $z$  as the coordinate along the cavity axis and by setting  $z = 0$  as the position of the cavity waist, the phase of a mode propagating along the cavity axis is given by  $\frac{2\pi}{\lambda}z - \Phi_G(z)$ , where  $\Phi_G(z) = \arctan\left(\frac{z}{z_R}\right)$  is the Gouy term with  $z_R = \frac{1}{2}\sqrt{L(2R - L)}$  the Rayleigh length. At the first order, the effective wavelength at the position  $z$  is then given by:

$$\lambda_i^{\text{eff}}(z) = \left( \frac{1}{\lambda_i} - \frac{1}{2\pi} \frac{d\Phi_G}{dz}(z) \right)^{-1}. \quad (1)$$

A maximal overlap is then obtained by the condition  $\lambda_2^{\text{eff}}(z) = 2\lambda_1^{\text{eff}}(z)$ .

This condition cannot be fulfilled for all  $z$  because the Gouy term is independent of the wavelength. By choosing to impose this condition at the waist ( $z = 0$ ) for a symmetric cavity, we obtain a relation between the wavelengths of the two modes:

$$\lambda_2^{\text{opt}} = \frac{2\lambda_1}{1 + \frac{\lambda_1}{2\pi z_R}}. \quad (2)$$

This simple relation guarantees a quasi-optimal overlap between the two effective wavelengths over a length smaller or comparable to  $z_R$  around the waist.

For our specific experiment,  $\lambda_1$  is the wavelength of the laser probe, which is fixed by the Rubidium atomic transition to 780.24 nm ( $D_2$  line of  $^{87}\text{Rb}$ ). The cavity mirrors have a radius of curvature  $R \approx 300 \mu\text{m}$  and the cavity length is  $L \approx 130 \mu\text{m}$ . From Eq. 2, we then get  $\lambda_2^{\text{opt}} \approx 1558.92 \text{ nm}$ , which is significantly different from  $2\lambda_1$ . This is due to the small value of the Rayleigh length  $z_R \approx 124 \mu\text{m}$  and the difference  $\lambda_2^{\text{opt}} - 2\lambda_1$  can exceed the tunability range

of typical diode lasers. Using this value for  $\lambda_2$ , we also calculate in the extreme off-centered position  $z = 65 \mu\text{m}$ , the ratio  $\lambda_2^{\text{eff}}/\lambda_1^{\text{eff}} \approx 1.99956$ , which indicates a good match between the effective wavelengths over the whole cavity length.

## 2.2. Doubly-resonant cavities

The cavity has to be simultaneously resonant at the two different wavelengths  $\lambda_1$  and  $\lambda_2$ . The eigenfrequencies of such a resonator are fixed by the condition that the phase shift accumulated in one cavity round-trip has to be an integer multiple of  $2\pi$ :

$$2\pi\nu_{qlp} \frac{2L}{c} - 2\phi_m - 4(l+p+1)\Phi_G\left(\frac{L}{2}\right) = 2\pi q \quad (3)$$

where  $\nu_{qlp}$  is the frequency of the eigenmode with longitudinal order  $q$  and whose Hermite-Gauss transverse shape is identified by  $l$  and  $p$ . As we will focus on the fundamental transverse mode TEM<sub>00</sub>, we set  $l = p = 0$ .  $\phi_m$  is the phase shift due to the reflection on a mirror, whose value is determined by the structure of the reflective coating.  $\Phi_G\left(\frac{L}{2}\right) = \arctan\left(\frac{L}{2z_R}\right)$  is the Gouy phase-shift accumulated from the center of the cavity to a mirror. One should note that the terms  $\phi_m$  and  $\Phi_G\left(\frac{L}{2}\right)$ , which are fixed for a given cavity, can significantly affect the resonant frequencies in the case of microcavities (where  $q$  is small).

For a doubly-resonant cavity, the condition of Eq. 3 has to be fulfilled by both wavelengths:

$$\begin{aligned} 2L \frac{2\pi}{\lambda_1} - 2\phi_{m1} - 4\Phi_G\left(\frac{L}{2}\right) &= 2\pi q_1 \\ 2L \frac{2\pi}{\lambda_2} - 2\phi_{m2} - 4\Phi_G\left(\frac{L}{2}\right) &= 2\pi q_2 \end{aligned} \quad (4)$$

where we have considered only the fundamental TEM<sub>00</sub> modes with longitudinal index  $q_1$  for  $\lambda_1$  and  $q_2$  for  $\lambda_2$ .  $\phi_{m1}$  and  $\phi_{m2}$  represents the phase shifts after a reflection on the mirror for the wavelengths  $\lambda_1$  and  $\lambda_2$ , respectively.

## 2.3. Optimal relative phase

The condition  $\lambda_2^{\text{eff}}(z) = 2\lambda_1^{\text{eff}}(z)$  is necessary but not sufficient to obtain a maximal spatial overlap between the standing waves of the two cavity modes. Indeed, even if the effective wavelengths  $\lambda_1^{\text{eff}}$  and  $\lambda_2^{\text{eff}}$  are commensurate, the relative position of the nodes of the standing waves inside the cavity is not univocal.

We first consider the simple configuration of a cavity with planar identically-coated mirrors which forces the condition  $\lambda_2 = 2\lambda_1$ . The symmetry imposes that each standing wave must have either a node or an antinode in the center of the cavity. Thus, only four configurations are possible, as shown in Fig. 2. The targeted configurations A and B, where the antinodes overlap, are only obtained if  $\lambda_1$  has an antinode in the center of the cavity. Whether the nodes of the standing waves (minimum overlap) or their antinodes (maximum overlap) are coincident is determined by the relative phase shift at reflection between the two wavelengths. In the following, we define the relative phase shift as  $\Delta\phi_m = \phi_{m2} - \frac{\phi_{m1}}{2}$ . As shown by the difference between the field intensities on the mirror for  $\lambda_2$  and  $\lambda_1$ , the four configurations have indeed different relative phase shifts at reflection.

By using the double resonance condition of Eqs. 4, we get the expression of the relative phase shift at reflection:

$$\Delta\phi_m \equiv \phi_{m2} - \frac{\phi_{m1}}{2} = \pi \left( \frac{q_1}{2} - q_2 \right) + 2\pi L \left( \frac{1}{\lambda_2} - \frac{1}{2\lambda_1} \right) - \Phi_G\left(\frac{L}{2}\right). \quad (5)$$

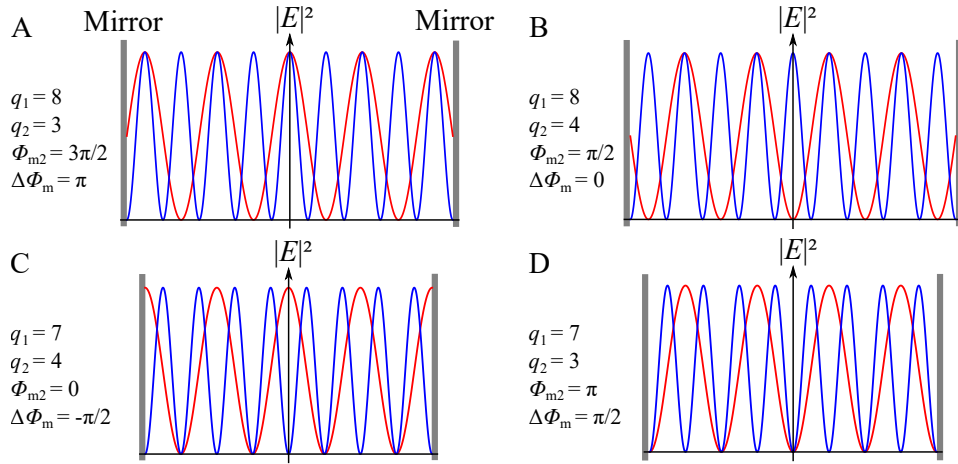


Fig. 2. Schematic view of the cavity field intensities  $|E|^2$  for the wavelengths  $\lambda_1$  (blue) and  $\lambda_2$  (red). Assuming that the two wavelengths differ by a factor 2, we show the four possible spatial configurations (A to D) that are allowed by symmetry in a cavity with planar mirrors and with a phase shift  $\phi_{m1} = \pi$  at reflection for  $\lambda_1$ . The parameters of the longitudinal indices  $q_1$  and  $q_2$ , the phase shifts  $\phi_{m2}$  at reflection for  $\lambda_2$  and the relative phase shifts at reflection  $\Delta\phi_m$ , specific to each configuration, are indicated in the graphs. The desired configurations A and B maximize the standing-waves overlap. The decaying field intensities inside the mirror are not shown here (see Fig. 5 for an example).

The four solutions presented in Fig. 2 are defined by the four integer and half-integer values of the quantity  $\frac{q_1}{2} - q_2$  modulo 2. Indeed, for a cavity with planar mirrors, the last two terms in Eq. 5 cancel because we impose  $\lambda_2 = 2\lambda_1$  from Eq. 2 and  $\Phi_G(\frac{L}{2}) = 0$ . The configurations presented in Fig. 2 assume  $\phi_{m1} = \pi$  to obtain a node on the mirror, and so  $q_1 + 1$  is the number of antinodes of the standing wave at  $\lambda_1$  in the cavity. Thus, there is an antinode in the center of the cavity when  $q_1$  is even, which corresponds to the configurations A and B. As a consequence, the maximal overlap of antinodes is obtained for  $\Delta\phi_m = (\frac{q_1}{2} - q_2)\pi$  with  $\frac{q_1}{2} - q_2$  integer. The solutions with  $\frac{q_1}{2} - q_2$  half-integer lead to overlapping nodes configurations C and D and must be rejected.

We can rewrite Eq. 5 by keeping only the optimal solutions and by reporting the condition for the wavelength  $\lambda_2 = \lambda_2^{\text{opt}}$  of Eq. 2 to get the optimal relative phase shift in the general case of a cavity with identical concave mirrors:

$$\Delta\phi_m^{\text{opt}} = n\pi + \delta\phi_m^{\text{opt}}, \quad \text{with} \quad \delta\phi_m^{\text{opt}} \equiv \left( \frac{L}{2z_R} - \arctan\left(\frac{L}{2z_R}\right) \right), \quad (6)$$

where  $n$  is an integer and where the non-integer part  $\delta\phi_m^{\text{opt}}$  of the relative phase depends only on two parameters : the cavity length  $L$  and the radius of curvature  $R$  of the mirrors. This non-integer part originates from the Gouy phase after compensation of its linear effect by the choice of  $\lambda_2^{\text{opt}}$ . For our specific cavity parameters, we get  $\delta\phi_m^{\text{opt}} = +2.4^\circ$ , which is a small value because the Rayleigh length  $z_R \approx 124 \mu\text{m}$  is on the order of the cavity length  $L$ .

The electric field amplitude  $E_i$  of the standing-wave at  $\lambda_i$  ( $i = 1, 2$ ) on the optical axis  $z$  is proportional to  $\cos(\Psi_i(z))$ , where the propagation phase  $\Psi_i$  is given by:

$$\Psi_i(z) = \frac{2\pi}{\lambda_i} \left( z - \frac{L}{2} \right) - \left( \Phi_G(z) - \Phi_G\left(\frac{L}{2}\right) \right) + \frac{\phi_{mi}}{2}. \quad (7)$$

Thus, the overlap between the two resonant cavity modes can be quantified by the overlap phase  $\Delta\Psi(z) = 2\Psi_2(z) - \Psi_1(z)$ , which indicates the dephasing between the two standing wave

patterns. Indeed, in case of perfect overlap, at the position of an antinode of the  $\lambda_2$  standing-wave, there is an antinode of the  $\lambda_1$  standing-wave, which implies that  $\Psi_2$  and  $\Psi_1$  are zero modulo  $\pi$ , as well as  $\Delta\Psi$ . On the contrary, if a node of the  $\lambda_1$  standing-wave is located at an antinode of the  $\lambda_2$  standing-wave, the overlap phase is  $\Delta\Psi = \pm\pi/2$  modulo  $\pi$ . As we seek to maintain the overlap over all the antinodes of the  $\lambda_2$  standing-wave,  $\Delta\Psi$  has to remain close to zero modulo  $\pi$  along the cavity axis  $z$ .

For a given relative phase on reflection  $\Delta\phi_m = n\pi + \delta\phi_m$  (with  $n$  integer and  $\delta\phi_m \in [-\pi/2, \pi/2]$ ) and a given wavelength  $\lambda_1$ , the condition of double resonance of Eqs. 4 imposes the wavelength  $\lambda_2$ , chosen to satisfy the condition  $\frac{q_1}{2} - q_2$  integer by using  $\frac{q_1}{2} - q_2 = n$  in order to be the closest of the optimal value  $\lambda_2^{\text{opt}}$  given by Eq. 2. By substituting the expressions of  $\lambda_1$  and  $\lambda_2$  in Eq. 7, we deduce the following expression of the overlap phase between the two resonant cavity modes :

$$\Delta\Psi(z) = \frac{z}{L/2}\delta\phi_m + n\pi + \frac{z}{L/2}\Phi_G(L/2) - \Phi_G(z) . \quad (8)$$

We see in this equation that the overlap phase depends explicitly on  $\delta\phi_m$  and so on the relative phase. In this equation, the  $n\pi$  term modulo  $2\pi$  differentiates between the solutions with antinodes overlapping at  $z = 0$  (type A in Fig. 2) or at  $z = \lambda_1^{\text{eff}}/2$  (type B in Fig. 2) which can both lead to optimal overlap if  $\delta\phi_m = \delta\phi_m^{\text{opt}}$ . As the overlap only depends on  $\Delta\Psi$  modulo  $\pi$ , we consider the case  $n = 0$ , where  $\Delta\phi_m = \delta\phi_m$ , for simplicity in the following analysis.

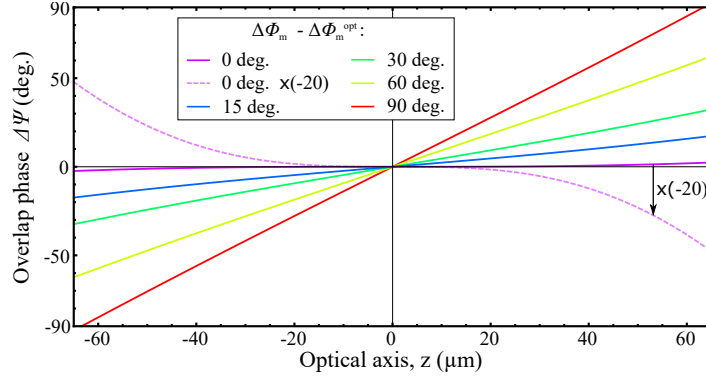


Fig. 3. Overlap phase  $\Delta\Psi$  between the standing waves at  $\lambda_1 = 780.24$  nm and  $\lambda_2$  along the cavity optical axis  $z$ , ranging over the full cavity length. Different colors correspond to different relative phases on reflection  $\Delta\phi_m$ , compared to the optimum value  $\Delta\phi_m^{\text{opt}}$ . The dashed light purple curve represent the optimal-phase purple curve multiplied by a factor  $-20$  to enhance the visibility.

In Fig. 3, we plot the overlap phase  $\Delta\Psi(z)$  for our specific cavity parameters, depending on the deviation  $\Delta\phi_m - \Delta\phi_m^{\text{opt}}$  from the optimal relative phase at reflection. In the general case where the relative phase  $\Delta\phi_m$  is not optimized, the overlap phase is dominated by the first term of Eq. 8 and we can observe in Fig. 3 a linear variation of  $\Delta\Psi(z)$  with a slope proportional to the relative phase on reflection. At the optimal relative phase  $\Delta\phi_m^{\text{opt}}$ , the overlap phase  $\Delta\Psi(z)$  is simply given by

$$\Delta\Psi(z) = \frac{z}{z_R} - \arctan\left(\frac{z}{z_R}\right) + n\pi. \quad (9)$$

Around  $z = 0$ , the choice of the optimum relative phase cancels at first order the  $z$  dependency of the overlap phase, which remains close to zero over the largest possible cavity length, meaning that the antinodes of the two standing waves coincide. Even at this optimal relative phase, a perfect overlap cannot be maintained over the whole cavity range due to the change in effective

wavelengths implied by the Gouy phase. However, in this case, the deviation has a zero derivative in the center of the cavity.

#### 2.4. Single atom-photon coupling along the atomic array

In CQED experiments, the strong coupling regime is reached when the single atom - single photon coupling strength  $g$  is larger than the cavity decay rate  $\kappa$  and the atomic one  $\gamma$ . For our specific atom and cavity,  $\gamma/(2\pi) \simeq 3$  MHz and  $\kappa/(2\pi) \simeq 15$  MHz. For an atom precisely positioned at an antinode (at the center of the cavity) of the standing wave of the resonant wavelength  $\lambda_1$ , we calculate the maximal value of the coupling strength  $g_{max}/(2\pi) \simeq 82$  MHz, indicating that our system operates deeply in the strong coupling regime of CQED.

To underline the need of carefully optimizing the overlap between the standing waves, we compute the single-atom single-photon coupling strength  $g$  at each trapping site (determined by the antinodes of the standing-wave of the  $\lambda_2$  mode) along the cavity axis  $z$  (see Fig.4). The calculation uses our specific cavity parameters and values of the dipole trap depth and the atom temperature, that are typically used in experiments. We plot the calculated coupling strength for different values of  $\Delta\phi_m - \Delta\phi_m^{opt}$ . At the center of the cavity where the two standing waves are overlapped, the calculated coupling strength  $g/(2\pi) \simeq 67$  MHz is reduced compared to the maximal one due to thermal motion of the atoms in the trap wells, which leads to an averaged value of  $g$ .

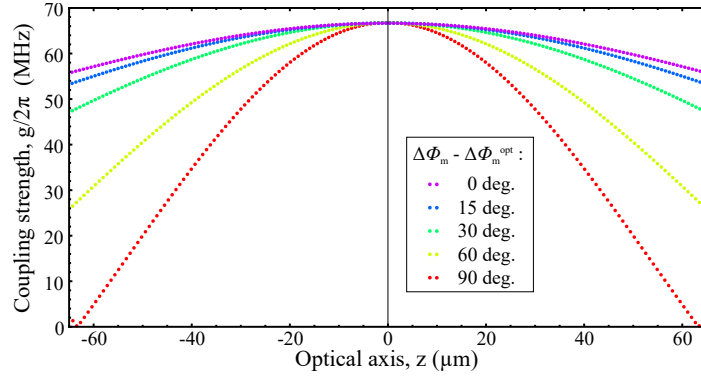


Fig. 4. Calculated coupling strength  $g/2\pi$  between a single atom and a single photon in the cavity field as a function of the position  $z$  of the lattice site where the atom is trapped, ranging over the full cavity length. Different colors correspond to different relative phases  $\Delta\phi_m$ , compared to the optimum value  $\Delta\phi_m^{opt}$ . The coupling has been calculated with: a cavity length  $L = 130 \mu\text{m}$ , mirrors with radius of curvature  $R = 300 \mu\text{m}$ , a cavity finesse  $\mathcal{F}_{780} = 5 \cdot 10^4$ , an intracavity circulating power of 100 mW for the dipole trap creating a maximal depth of  $72 \mu\text{K}$ , and a temperature of the atom of  $10 \mu\text{K}$ .

As the relative phase  $\Delta\phi_m$  approaches the optimal one, the variation of the coupling along  $z$  becomes dominated by the divergence of the cavity mode at 780 nm, with a coupling difference between the center and the periphery of the cavity below 15%. In the opposite case, if the relative phase  $\Delta\phi_m$  deviates from the optimal one, the coupling decreases strongly while moving away from the cavity center. In the limit of a  $90^\circ$  deviation, the coupling decreases to half of the maximal value at  $40 \mu\text{m}$  from the center. This underlines the importance of implementing and verifying experimentally the conditions described above for achieving an optimal overlap between the cavity standing waves.



### 3. Dual-wavelength reflective coating

As explained in the previous section, the relative phase at the reflection on a cavity mirror is a crucial parameter to obtain the maximal overlap. In this section, we discuss the implementation of the relative phase for the high reflective dielectric coating used for our fiber mirrors [35].

Our mirrors are Bragg reflectors obtained by stacking layers of different dielectric materials, deposited on the end facet of the fiber by ion sputtering. The Bragg structure determines not only the global reflection and transmission coefficients of the mirrors, but also the relative phase shift at reflection between  $\lambda_1$  and  $\lambda_2$ , which is essential for the optimal overlap between the standing waves. The company Laseroptik designed and realized the mirror coating taking into account the given constraint of the relative phase at reflection. The expected optical properties of our mirrors solely depend on the thickness and the optical index of the different Bragg layers, resulting in the optical index profile shown in Fig. 5. We performed a calculation of the optical field based on the evolution of an incident scalar plane wave in the transfer matrix formalism [36] for each wavelength  $\lambda_1 = 780$  nm and  $\lambda_2 = 1559$  nm, see Fig. 5.

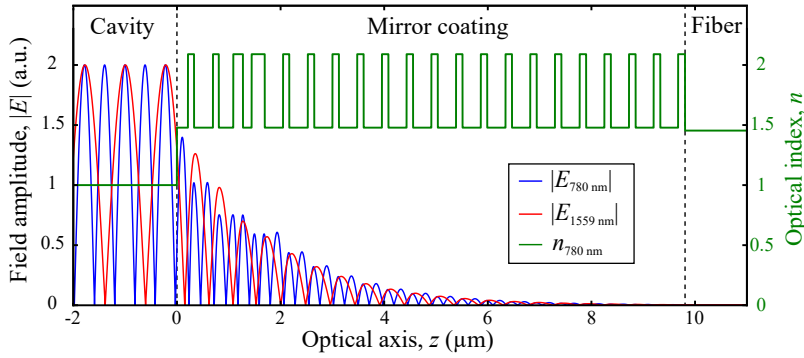


Fig. 5. Calculation of the mirror properties. The green curve shows the evolution of optical index  $n$  along the optical axis  $z$ , inside the dielectric mirror (starting at  $z = 0$ , dashed lines shows the mirror stack limits). The electric field amplitudes  $|E|$  of reflected waves at 780 nm and 1559 nm are represented in blue and red, respectively. They are calculated with transfer matrix theory from the optical index and assuming an incident wave of amplitude 1.

We observe that the fields decrease quickly while penetrating in the mirror because the layers reflect progressively the incident wave. From the field energy distribution, we calculate the optical penetration depths  $d_{p,1} \approx 1.20 \mu\text{m}$  and  $d_{p,2} \approx 1.51 \mu\text{m}$ , at  $\lambda_1 = 780$  nm and  $\lambda_2 = 1559$  nm, respectively. The penetration of the field in the mirrors increases the effective optical length of the cavity  $L_{\text{eff}} = L + 2d_p$ , which defines the free spectral range (FSR)  $c/2L_{\text{eff}}$ . In the calculations of the previous sections (Eq. 3 and resulting equations), the propagation phase accumulated in the penetration depth by the wave is included in the mirror reflection phase  $\phi_m$ . By using the resonance condition of Eq. 3 to calculate the FSR and by linearizing in the FSR expression the change of the reflection phase  $\phi_m(\lambda)$  with the wavelength  $\lambda$ , the penetration depth can also be calculated as  $d_{p,i} \approx \frac{\lambda_i^2}{4\pi} \frac{\partial \phi_m}{\partial \lambda}(\lambda_i)$ . This calculation of the penetration depth is analytically equivalent to the one using the energy field distribution for high reflective Bragg mirrors [37]. Indeed, when applied to our calculated mirror phases at  $\lambda_1 = 780$  nm and  $\lambda_2 = 1559$  nm, this equation yields the same values of penetration depths than the ones obtained from the field energy distribution.

In Fig. 5, we also directly observe that the field antinodes of the two standing waves have a very good spatial overlap. From the field calculations, we find that the fields at  $\lambda_1$  and  $\lambda_2$  have reflection phases  $\phi_{m,1} = 207.6^\circ$  and  $\phi_{m,2} = 99.4^\circ$  respectively, and thus a relative phase

$\Delta\phi_m = 0 \times \pi + \delta\phi_m$  with  $\delta\phi_m = -4.4^\circ$ . This value differs from the optimal value of  $+2.4^\circ$  calculated above from our cavity parameters. The reason for this discrepancy is incidental and it originates from a different convention used by the coating company in considering the sign of the phase. However, this deviation from the optimum is small and thus the overlap is still nearly optimal, with the coupling strength at each trapping site varying by less than 0.3% from the values of the optimal relative phase configuration (cf. Fig. 4).

In the following paragraphs, we present two methods that allow us to confirm the calculation by measuring the relative phase shift at reflection between the cavity modes at  $\lambda_1$  and  $\lambda_2$ . The first one is a direct visualization of the standing waves, allowing to distinguish the configurations of maximal and minimal overlap (Fig. 2), *i.e.* to get the integer contribution to  $\Delta\phi_m$  (modulo  $2\pi$ ). The second technique consists in a measurement of the precise value of the phase difference by estimating  $\delta\phi_m$ .

#### 4. Measurement of the overlap of cavity standing waves with a tapered fiber tip

We directly visualize the cavity standing waves with the method described in Ref. [38]. We use a tapered fiber tip with sub-wavelength apex size to perturb the cavity modes, see Fig. 6(a). We measure the additional losses induced by the tip from the change of cavity transmission. When the tip is displaced along the cavity optical axis  $z$ , the tip-induced losses change periodically between a maximum value, when the tip is at the antinodes of the cavity standing waves, and a minimum value, when the tip is at the nodes. In Fig. 6(b), we show the result of two sweeps of the tip along a few periods of the standing waves along the cavity axis  $z$ : one for each wavelength  $\lambda_1$  and  $\lambda_2$ . The two sweeps are performed at different depth of the tip inside the mode, corresponding to the two optimal positions for the signal-to-noise, as described in Ref. [38].

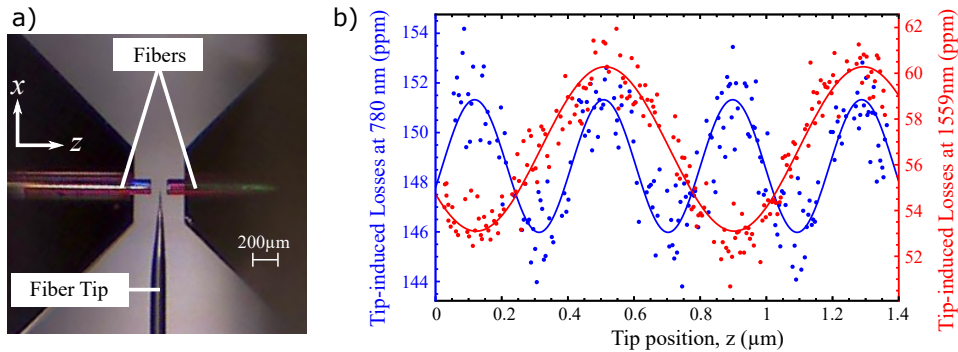


Fig. 6. (a): Image of the fiber tip inserted in the fiber cavity for the measurement of the overlap between optical standing waves. (b): Tip-induced cavity losses (data points) at  $\lambda_1$  and  $\lambda_2$  as a function of the tip position  $z$  along the cavity axis. The solid curves are best-fit sinusoids.

In Fig. 6(b), the maxima of the losses at  $\lambda_1$  and  $\lambda_2$  coincide, which is the signature that the spatial configuration of the standing waves is the one maximizing the overlap between the antinodes ( $\frac{q_1}{2} - q_2$  integer), and not the one where the nodes are coincident ( $\frac{q_1}{2} - q_2$  half-integer). The sinusoidal fit functions give the difference between the fitted positions of the antinodes at  $\lambda_2$  and  $\lambda_1$  of about 1 nm, which is below the uncertainty of our alignment procedure of about  $\pm 30$  nm [38]. Knowing that the tip was positioned at about  $40 \mu\text{m}$  from the center of the cavity and that increasing  $z$  corresponds to a movement towards the mirror, we obtain a rough estimation of the relative phase shift at the reflection:

$$\Delta\phi_m = n\pi + \delta\phi_m \quad \text{with } n \text{ integer} \quad \text{and} \quad \delta\phi_m = (-1 \pm 25)^\circ. \quad (10)$$

A complementary measurement, presented in the next section, allows us to estimate  $\delta\phi_m$  with a much better precision, using the result obtained here that  $n$  is an integer.

## 5. Precise measurement of the relative phase shift at reflection

We implement a method for measuring with a better precision the relative phase shift  $\delta\phi_m$ . The procedure consists in measuring the laser frequency  $\nu_2 = c/\lambda_2$  for which the cavity is simultaneously resonant at  $\nu_2$  and at  $\nu_1 = c/\lambda_1$  (which is kept fixed) for different cavity lengths. As we will show in the following, the variation of the laser frequency  $\nu_2(L)$  as a function of the cavity  $L$  depends strongly on the relative phase at reflection.

Starting from the condition of simultaneous resonance of Eq. 4, we divide by 2 the equation for  $\lambda_1$  and subtract it from the one for  $\lambda_2$ , we obtain:

$$\frac{2L}{c}2\pi\nu_2 = \frac{2L}{c}2\pi\frac{\nu_1}{2} + 2\Phi_G\left(\frac{L}{2}\right) + 2\Delta\phi_m - 2\pi\left(\frac{q_1}{2} - q_2\right). \quad (11)$$

By inserting in this equation, the relative phase as  $\Delta\phi_m = n\pi + \delta\phi_m$  with  $n$  integer or half-integer and  $\delta\phi_m \in [-\pi/4, \pi/4]$ , we obtain:

$$\nu_2(L) = \frac{\nu_1}{2} + \frac{c}{2L}\frac{1}{\pi}\left(\Phi_G\left(\frac{L}{2}\right) + \delta\phi_m\right) + \frac{c}{2L}\left(n - \left(\frac{q_1}{2} - q_2\right)\right) \quad (12)$$

In this expression, the last term, which contains the  $n\pi$ -term of the relative phase, cancels because experimentally we choose  $\frac{q_1}{2} - q_2 = n$  such that the frequency  $\nu_2$  is the closest possible to  $\nu_1/2$  to get  $\lambda_2 \simeq \lambda_2^{\text{opt}} \simeq 2\lambda_1$ . Due to this effect, the measurement method, we will present below, only allows to determine the value of non integer part  $\delta\phi_m$  of the relative phase. As we know from the fiber tip measurement presented before that  $n$  is an integer, we can determine unambiguously  $\Delta\phi_m$  modulo  $\pi$ , and so the overlap between the coupling and trapping standing waves. Without a direct measurement of the standing waves overlap, this method can still be used in combination with a calculation of the optical field taking account the parameters of the Bragg layers of the mirrors (see Sect. 3).

By writing explicitly the expression of the Gouy phase and the Rayleigh length, we find:

$$\nu_2(L) = \frac{\nu_1}{2} + \frac{c}{2L}\frac{1}{\pi}\left(\arctan\left(\sqrt{\frac{L}{2R-L}}\right) + \delta\phi_m\right) \quad (13)$$

This variation of the frequency  $\nu_2$  necessary to maintain the double resonance condition while keeping  $\nu_1$  fixed is plotted in Fig. 7(a) as function of the cavity length  $L$  for different values of  $\delta\phi_m$ . We clearly observe that small differences in the value of  $\delta\phi_m$  lead to strongly different curves, thus allowing for high precision measurement of the relative phase shift at reflection.

Experimentally, the frequency  $\nu_1 = 384.228$  THz is fixed by tuning a 780 nm laser diode to a given transition of a saturated-absorption spectroscopy signal of the rubidium  $D_2$  line. The frequency  $\nu_2$  of a 1559 nm laser diode is controlled by adjusting the current or the temperature of the laser diode. To observe the cavity resonances, we measure the cavity transmission while modulating the cavity length with an amplitude of approximately  $\lambda_1$  with a piezoelectric actuator. At the double resonance, both transmissions of the 780 nm laser and 1559 nm laser are maximum for the same voltage on the piezoelectric actuator. In order to reach this situation, we adjust the frequency  $\nu_2$  of the 1559 nm laser to the closest double resonance from  $\nu_1/2$ . Starting with a cavity length of approximately 150  $\mu\text{m}$ , the length  $L$  of the cavity is progressively reduced by a micrometric screw with a resolution of  $\pm 0.5 \mu\text{m}$ . At every step,  $\nu_2$  is tuned in order to be simultaneously resonant with  $\nu_1$ . In order to know the frequency  $\nu_2$  of the 1559 nm laser, we interpolate the values of  $\nu_2$  provided by a spectrometer for different values of the current and the

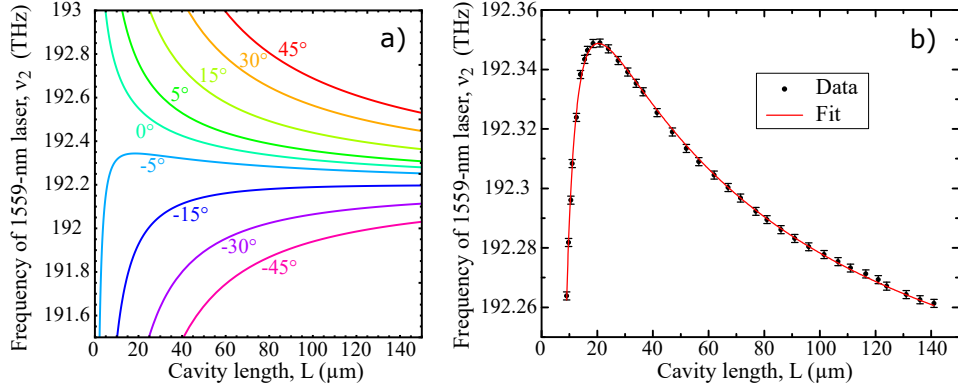


Fig. 7. Resonant frequency  $\nu_2$  of the 1559 nm laser for which the cavity is simultaneously resonant at  $\nu_1$  (fixed to rubidium D<sub>2</sub> line), as a function of the cavity length  $L$ . (a): Theoretical curves given by Eq. 13 for different values of  $\delta\phi_m$  (indicated in degree next to the curve). (b): Experimental data (black points) and best-fit curve (red) obtained with Eq. 13. The error bars on the frequency ( $\pm 1.4$  GHz) represent the precision of our laser frequency calibration; the precision of the relative cavity length of  $\pm 0.5 \mu\text{m}$  is not shown.

temperature, with a relative precision estimated to be 1.4 GHz. We repeat this procedure up to reach the shortest accessible value of the cavity length.

We obtain the data presented in Fig. 7(b), that we fit with the model of Eq. 13, knowing the average measured radius of curvature of the mirrors  $R \simeq 300 \mu\text{m}$ . Systematic errors on the measured values of the laser frequency  $\nu_2$  and of the cavity length  $L$  are taken into account by adding offsets that are free parameters for the fitting function  $\nu_2(L + \delta L) + \delta\nu_2$  where  $\nu_2$  is given by Eq. 13. The resulting fitted values  $\delta\nu_2 \simeq 3.6$  GHz and  $\delta L \simeq 2.2 \mu\text{m}$  are well below the accuracies of the spectrometer of 60 GHz and of the cavity length estimation of  $5 \mu\text{m}$ , respectively. As these additional fit parameters only lead to linear displacements of the curve, they do not affect the determination of the relative phase  $\delta\phi_m$  which controls the shape of the curve.

For our cavity, the phase  $\delta\phi_m$  is slightly negative; thus, in the expression of  $\nu_2$  (see Eq. 13), the term in  $\delta\phi_m/L$  is negative whereas the Gouy phase term is positive. The term in  $\delta\phi_m/L$  determines the divergence of  $\nu_2$  when  $L$  goes to zero, because it dominates the Gouy phase term which asymptotically diverges as  $1/\sqrt{L}$  when  $L \ll R$ . Thus, with our small negative relative phase, in Fig. 7(b) when the cavity length tends to zero, the frequency  $\nu_2$  is first dominated by a  $1/\sqrt{L}$  asymptotic behavior that leads to an increase towards higher values originating from the Gouy phase term, but eventually  $\nu_2$  diverges to smaller values of  $\nu_2$  due to the  $\delta\phi_m/L$  term.

From the fit, we find that the relative phase shift at reflection is  $\delta\phi_m = (-4.9 \pm 0.1)^\circ$ , assuming  $R = 300 \mu\text{m}$ . In our case, there is an additional  $\pm 10\%$  uncertainty on  $R$ , stemming from small deviations to spherical shape of our mirrors, which increases the uncertainty of  $\delta\phi_m$  to  $\pm 0.5^\circ$ . The measured value of the relative phase shift is in good agreement with the calculation based on the coating properties. We emphasize the excellent uncertainty obtained by our measurement method, which is a consequence of the high precision of the laser frequency measurement and of the translation stage that adjusts the cavity length.

## 6. Conclusion

In this article, we optimize the spatial overlap between commensurate standing waves in a doubly-resonant cavity. We derive two conditions that have to be fulfilled to optimize this overlap. First, the effective wavelength (including the Gouy phase) of the trapping lattice has to be commensurate with the effective wavelength of the mode that is strongly coupled to the

atoms. This implies that the wavelength  $\lambda_2$  of the trapping mode has to fulfill Eq. 2. We note that such an optimization is possible because we have some freedom in the choice of the the trapping wavelength  $\lambda_2$ , as opposed to frequency doubling experiments. Second, the antinodes of the two standing waves have to coincide, which is critically linked to the relative phase shift  $\Delta\phi_m$  at the reflection on the cavity mirrors. We calculate the expression of Eq. 6 of the optimal value of  $\Delta\phi_m$  as a function of the cavity parameters.

The relative phase is controlled by the design of the dielectric mirror and can be calculated with standard transfer matrix calculations. In order to experimentally check the overlap and measure  $\Delta\phi_m$ , we develop a two step method. First, the visualization of the optical field distribution with the fiber tip gives a direct measurement of the spatial overlap, which allows us to verify that the maxima of the cavity fields (and not the minima) are matched. Second, this result is completed by a more precise characterization of the relative phase, and therefore of the spatial overlap, by measuring the frequency  $\nu_2(L)$  of the dipole laser which satisfies the double resonance condition as a function of the cavity length  $L$ . Using this procedure, we could demonstrate that a nearly-optimal spatial overlap is achieved in our cavity.

Additionally, we note that a fiber Fabry-Perot cavity, using the same type of fibers and coatings, has been placed in an ultra-high vacuum chamber (in presence of Rubidium atoms), since two and a half year. The cavity finesse and the relative phase shift at reflection have remained constant during this time, thus avoiding degradation issues [39–41]. Photothermal effects [30, 42, 43] on the change of the relative phase shift are negligible ( $< 2 \cdot 10^{-3}$ ) with the 480-mW circulating power of the 1559-nm optical lattice, we maximally use to trap atoms. The excellent values and stabilities of both the finesse and the standing-wave overlap are essential features of our CQED setup.

The spatial overlap is a critical requirement to produce new atom-photon interfaces, where a strong and uniform coupling between the resonant cavity mode and each atom of the array is combined with single particle control. The spacing between trapping sites is indeed large enough to be resolvable by a high numerical aperture lens as described in Ref. [38]. This opens the way to new CQED experiments, where collective operations mediated by the cavity and local operations on each site of the lattice can be used to generate and study multi-particle entanglement. Such experiments can address the generation and characterization of entangled states delocalized over the entire atomic array, useful for multiparameter quantum-enhanced sensing [44, 45]. The control of a single atom of the array can be used to generate Schrödinger cat-state [46] or to perform controlled-string operation [47]. Finally, the control over the local coupling at each site between the atoms via the cavity field enable the simulation of specific spin models [19, 48].

## Funding

This work was supported by : Agence Nationale de la Recherche (ANR) (SAROCMA project, ANR-14-CE32-0002); European Research Council (ERC) under the European Union’s Horizon 2020 research and innovation programme Grant agreement No 671133 (EQUEMI project); and the DIM SIRTEQ from Région Ile-de-France.

## Acknowledgments

The authors acknowledge Pierre-Antoine Bourdel for careful reading of the manuscript and Tobias Gross (Laseroptik) for fruitful interaction and expert advice.

## Disclosures

The authors declare no conflicts of interest.

## References

1. S. Haroche and J.-M. Raimond, *Exploring the Quantum: Atoms, Cavities, and Photons* (Oxford University Press, 2006).
2. D. Meschede, H. Walther, and G. Müller, “One-Atom Maser,” *Phys. Rev. Lett.* **54**, 551–554 (1985).
3. G. Rempe, H. Walther, and N. Klein, “Observation of quantum collapse and revival in a one-atom maser,” *Phys. Rev. Lett.* **58**, 353–356 (1987).
4. M. Brune, F. Schmidt-Kaler, A. Maali, J. Dreyer, E. Hagley, J. M. Raimond, and S. Haroche, “Quantum Rabi Oscillation: A Direct Test of Field Quantization in a Cavity,” *Phys. Rev. Lett.* **76**, 1800–1803 (1996).
5. R. J. Thompson, G. Rempe, and H. J. Kimble, “Observation of normal-mode splitting for an atom in an optical cavity,” *Phys. Rev. Lett.* **68**, 1132–1135 (1992).
6. J. P. Reithmaier, G. Şek, A. Löffler, C. Hofmann, S. Kuhn, S. Reitzenstein, L. V. Keldysh, V. D. Kulakovskii, T. L. Reinecke, and A. Forchel, “Strong coupling in a single quantum dot–semiconductor microcavity system,” *Nature* **432**, 197–200 (2004).
7. T. Yoshie, A. Scherer, J. Hendrickson, G. Khitrova, H. M. Gibbs, G. Rupper, C. Ell, O. B. Shchekin, and D. G. Deppe, “Vacuum Rabi splitting with a single quantum dot in a photonic crystal nanocavity,” *Nature* **432**, 200–203 (2004).
8. A. Wallraff, D. I. Schuster, A. Blais, L. Frunzio, R.-S. Huang, J. Majer, S. Kumar, S. M. Girvin, and R. J. Schoelkopf, “Strong coupling of a single photon to a superconducting qubit using circuit quantum electrodynamics,” *Nature* **431**, 162–167 (2004).
9. S. Ritter, C. Nölleke, C. Hahn, A. Reiserer, A. Neuzner, M. Uphoff, M. Mücke, E. Figueroa, J. Bochmann, and G. Rempe, “An elementary quantum network of single atoms in optical cavities,” *Nature* **484**, 195–200 (2012).
10. J. Gallego, W. Alt, T. Macha, M. Martinez-Dorantes, D. Pandey, and D. Meschede, “Strong Purcell Effect on a Neutral Atom Trapped in an Open Fiber Cavity,” *Phys. Rev. Lett.* **121**, 173603 (2018).
11. M. H. Schleier-Smith, I. D. Leroux, and V. Vuletić, “States of an Ensemble of Two-Level Atoms with Reduced Quantum Uncertainty,” *Phys. Rev. Lett.* **104**, 073604 (2010).
12. R. McConnell, H. Zhang, J. Hu, S. Ćuk, and V. Vuletić, “Entanglement with negative Wigner function of almost 3,000 atoms heralded by one photon,” *Nature* **519**, 439–442 (2015).
13. O. Hosten, N. J. Engelsens, R. Krishnakumar, and M. A. Kasevich, “Measurement noise 100 times lower than the quantum-projection limit using entangled atoms,” *Nature* **529**, 505–508 (2016).
14. G. Barontini, L. Hohmann, F. Haas, J. Esteve, and J. Reichel, “Deterministic generation of multiparticle entanglement by quantum Zeno dynamics,” *Science* **349**, 1317–1321 (2015).
15. S. Welte, B. Hacker, S. Daiss, S. Ritter, and G. Rempe, “Cavity Carving of Atomic Bell States,” *Phys. Rev. Lett.* **118**, 210503 (2017).
16. K. Baumann, C. Guerlin, F. Brennecke, and T. Esslinger, “Dicke quantum phase transition with a superfluid gas in an optical cavity,” *Nature* **464**, 1301–1306 (2010).
17. M. Landini, N. Dogra, K. Kroeger, L. Hruby, T. Donner, and T. Esslinger, “Formation of a spin texture in a quantum gas coupled to a cavity,” *Phys. Rev. Lett.* **120**, 223602 (2018).
18. R. M. Kroeze, Y. Guo, V. D. Vaidya, J. Keeling, and B. L. Lev, “Spinor Self-Ordering of a Quantum Gas in a Cavity,” *Phys. Rev. Lett.* **121**, 163601 (2018).
19. E. J. Davis, G. Bentsen, L. Homeier, T. Li, and M. H. Schleier-Smith, “Photon-Mediated Spin-Exchange Dynamics of Spin-1 Atoms,” *Phys. Rev. Lett.* **122**, 010405 (2019).
20. Y. Colombe, T. Steinmetz, G. Dubois, F. Linke, D. Hunger, and J. Reichel, “Strong atom–field coupling for Bose–Einstein condensates in an optical cavity on a chip,” *Nature* **450**, 272–276 (2007).
21. F. Brennecke, T. Donner, S. Ritter, T. Bourdel, M. Köhl, and T. Esslinger, “Cavity QED with a Bose–Einstein condensate,” *Nature* **450**, 268–271 (2007).
22. R. Blatt and D. Wineland, “Entangled states of trapped atomic ions,” *Nature* **453**, 1008–1015 (2008).
23. S. de Léséleuc, V. Lienhard, P. Scholl, D. Barredo, S. Weber, N. Lang, H. P. Büchler, T. Lahaye, and A. Browaeys, “Observation of a symmetry-protected topological phase of interacting bosons with Rydberg atoms,” *Science* **365**, 775–780 (2019).
24. W. S. Bakr, J. I. Gillen, A. Peng, S. Fölling, and M. Greiner, “A quantum gas microscope for detecting single atoms in a Hubbard-regime optical lattice,” *Nature* **462**, 74–77 (2009).
25. R. Reimann, W. Alt, T. Kampschulte, T. Macha, L. Ratschbacher, N. Thau, S. Yoon, and D. Meschede, “Cavity-Modified Collective Rayleigh Scattering of Two Atoms,” *Phys. Rev. Lett.* **114**, 023601 (2015).
26. G. Vrijsen, O. Hosten, J. Lee, S. Bernon, and M. A. Kasevich, “Raman Lasing with a Cold Atom Gain Medium in a High-Finesse Optical Cavity,” *Phys. Rev. Lett.* **107**, 063904 (2011).
27. K. J. Arnold, M. P. Baden, and M. D. Barrett, “Self-Organization Threshold Scaling for Thermal Atoms Coupled to a Cavity,” *Phys. Rev. Lett.* **109**, 153002 (2012).
28. J. Lee, G. Vrijsen, I. Teper, O. Hosten, and M. A. Kasevich, “Many-atom–cavity QED system with homogeneous atom–cavity coupling,” *Opt. Lett.* **39**, 4005 (2014).

29. A. J. Kollár, A. T. Papageorge, K. Baumann, M. A. Armen, and B. L. Lev, “An adjustable-length cavity and Bose–Einstein condensate apparatus for multimode cavity QED,” *New J. Phys.* **17**, 043012 (2015).
30. D. Hunger, T. Steinmetz, Y. Colombe, C. Deutsch, T. W. Hänsch, and J. Reichel, “A fiber Fabry–Perot cavity with high finesse,” *New J. Phys.* **12**, 065038 (2010).
31. A. Ashkin, G. Boyd, and J. Dziedzic, “Resonant optical second harmonic generation and mixing,” *IEEE J. Quantum Electron.* **2**, 109–124 (1966).
32. L.-A. Wu and H. J. Kimble, “Interference effects in second-harmonic generation within an optical cavity,” *J. Opt. Soc. Am. B* **2**, 697 (1985).
33. R. Paschotta, K. Fiedler, P. Kürz, and J. Mlynek, “Nonlinear mode coupling in doubly resonant frequency doublers,” *Appl. Phys. B* **58**, 117–122 (1994).
34. M. Liscidini and L. Claudio Andreani, “Second-harmonic generation in doubly resonant microcavities with periodic dielectric mirrors,” *Phys. Rev. E* **73**, 016613 (2006).
35. S. Garcia, F. Ferri, K. Ott, J. Reichel, and R. Long, “Dual-wavelength fiber Fabry-Perot cavities with engineered birefringence,” *Opt. Express* **26**, 22249 (2018).
36. S. A. Furman and A. V. Tikhonravov, *Basics of Optics of Multilayer Systems* (Atlantica Séguier Frontières, 1992).
37. D. I. Babic and S. W. Corzine, “Analytic expressions for the reflection delay, penetration depth, and absorptance of quarter-wave dielectric mirrors,” *IEEE J. Quantum Electron.* **28**, 514–524 (1992).
38. F. Ferri, S. Garcia, M. Baghdad, J. Reichel, and R. Long, “Mapping optical standing-waves of an open-access fabry-perot cavity with a tapered fiber,” *Rev. Sci. Instrum.* (accepted for publication) (2020).
39. B. Brandstätter, A. McClung, K. Schüppert, B. Casabone, K. Friebe, A. Stute, P. O. Schmidt, C. Deutsch, J. Reichel, R. Blatt, and T. E. Northup, “Integrated fiber-mirror ion trap for strong ion-cavity coupling,” *Rev. Sci. Instruments* **84**, 123104 (2013).
40. D. Gangloff, M. Shi, T. Wu, A. Bylinskii, B. Braverman, M. Gutierrez, R. Nichols, J. Li, K. Aichholz, M. Cetina, L. Karpa, B. Jelenković, I. Chuang, and V. Vuletić, “Preventing and reversing vacuum-induced optical losses in high-finesse tantalum (v) oxide mirror coatings,” *Opt. Express* **23**, 18014–18028 (2015).
41. J. Schmitz, H. M. Meyer, and M. Köhl, “Ultraviolet fabry-perot cavity with stable finesse under ultrahigh vacuum conditions,” *Rev. Sci. Instruments* **90**, 063102 (2019).
42. J. F. S. Brachmann, H. Kaupp, T. W. Hänsch, and D. Hunger, “Photothermal effects in ultra-precisely stabilized tunable microcavities,” *Opt. Express* **24**, 21205–21215 (2016).
43. K. Konthasinghe, J. G. Velez, A. J. Hopkins, M. Peiris, L. T. M. Profeta, Y. Nieves, and A. Muller, “Self-sustained photothermal oscillations in high-finesse fabry-perot microcavities,” *Phys. Rev. A* **95**, 013826 (2017).
44. T. Baumgratz and A. Datta, “Quantum Enhanced Estimation of a Multidimensional Field,” *Phys. Rev. Lett.* **116**, 030801 (2016).
45. M. Gessner, L. Pezzè, and A. Smerzi, “Sensitivity Bounds for Multiparameter Quantum Metrology,” *Phys. Rev. Lett.* **121**, 130503 (2018).
46. C. C. Gerry and R. Grobe, “Generation and properties of collective atomic schrödinger-cat states,” *Phys. Rev. A* **56**, 2390–2396 (1997).
47. L. Jiang, G. K. Brennen, A. V. Gorshkov, K. Hammerer, M. Hafezi, E. Demler, M. D. Lukin, and P. Zoller, “Anyonic interferometry and protected memories in atomic spin lattices,” *Nat. Phys.* **4**, 482–488 (2008).
48. G. Bentsen, T. Hashizume, A. S. Buyskikh, E. J. Davis, A. J. Daley, S. S. Gubser, and M. Schleier-Smith, “Treelike Interactions and Fast Scrambling with Cold Atoms,” *Phys. Rev. Lett.* **123**, 130601 (2019).